Measurement of the x-ray mass attenuation coefficient of copper using 8.85–20 keV synchrotron radiation

C. T. Chantler,[1] C. Q. Tran,[1] Z. Barnea,[1] D. Paterson,[1] D. J. Cookson,[2] and D. X. Balaic[1]
[1]*School of Physics, University of Melbourne, Victoria 3010, Australia*
[2]*ANSTO, Private Mail Bag 1, Menai, NSW 2234, Australia*
and Chem-Mat-CARS-CAT (Sector 15, Bldg 434D), Argonne National Laboratory, 9700 S. Cass Avenue, Argonne, Illinois 60439
(Received 27 June 2001; published 19 November 2001)

This work presents the x-ray extended range technique for measuring x-ray mass attenuation coefficients. This technique includes the use of multiple foil attenuators at each energy investigated, allowing independent tests of detector linearity and of the harmonic contributions to the monochromated synchrotron beam. Measurements over a wide energy range allow the uncertainty of local foil thickness to be minimized by the calibration of thin sample measurements to those of thick samples. The use of an extended criterion for sample thickness selection allows direct determination of dominant systematics, with an improvement of accuracies compared to previous measurements by up to factors of 20. Resulting accuracies for attenuation coefficients of copper (8.84 to 20 keV) are 0.27–0.5 %, with reproducibility of 0.02%. We also extract the imaginary component of the form factor from the data with the same accuracy. Results are compared to theoretical calculations near and away from the absorption edge. The accuracy challenges available theoretical calculations, and observed discrepancies of 10% between current theory and experiments can now be addressed.

DOI: 10.1103/PhysRevA.64.062506 PACS number(s): 32.30.Rj, 32.80.Fb, 61.10.Ht, 61.10.Eq

I. INTRODUCTION

A precise understanding of the way x-ray photons interact with matter is important in atomic physics, crystallography, medical diagnosis, and surface and material sciences. Recent major developments have concentrated on applications for structural determination near absorption edges, including the use of Bijvoet ratios [1], multiple-wavelength anomalous dispersion (MAD) techniques [2], x-ray absorption fine structure (XAFS) investigations [3], and diffraction anomalous fine structure (DAFS) [4].

The complex form factor f (the resonant scattering amplitude of x rays due to the charge distribution), is the fundamental parameter for all optical devices. It specifies refractive indices, permittivities, scattering, and attenuation coefficients, and hence the critical properties for mirrors, lenses, filters, and coatings. In the x-ray regime, the form factor becomes accessible to theoretical prediction on the basis of atomic physics and the atomic form factor [5]. At intermediate x-ray energies, photons are primarily attenuated or elastically scattered by matter. Inelastic scattering becomes dominant only at higher energies (above 40 keV for copper).

Current computations of theories vary by many quoted standard deviations from one another in important regions [6,7]. In some cases this variation is due to a lack of convergence of the computation; in other cases it is due to inadequate assumptions relating to the wave functions. This is a difficult area to compare directly with experiment, since experimental data must be obtained to high accuracy over extended ranges of energy and attenuation to observe both structural variation and possible offsets due to any given assumptions. This work presents the results of such an extended investigation.

The imaginary component of the form factor $\mathrm{Im}(f)$ may be determined from studies of the full complex form factor using x-ray interferometry [8,9], reflection and refraction [10,11], diffraction intensities [12,13], and pendellösung fringes [14,15]. Some difficulties of these approaches include the often narrow energy range covered by interferometric methods, the limited accuracy of separating the imaginary component of f from the real component in measurements of the full structure factor for a solid, and assumptions in using the Kramers-Kronig relation on a limited data set of $\mathrm{Re}(f)$ measurements.

Alternatively, $\mathrm{Im}(f)$ (denoted by f'' or f_2 by various authors) may be related directly to the photoelectric absorption coefficient and, equivalently, the photoelectric absorption cross section σ_{PE}, by the energy E, the classical electron radius r_e, Planck's constant h, and the speed of light c,

$$\mathrm{Im}(f)=f''(E)=f_2(E)=\frac{E\sigma_{PE}}{2hcr_e}. \tag{1}$$

Compilations of experimental data of σ_{PE} over the last decade show large variations of up to 30%, although many authors have claimed 1% precision or better using various experimental techniques [16,17]. These variations are due to unresolved systematics relating to sample thickness determination and purity, detector linearity, harmonic contamination of the x-ray beam, scattering, energy calibration, and beam divergence. The most reliable results quoted in the literature relate to the work of Creagh and Hubbell [17], Gerward [18], and Mika *et al.* and Chantler and Barnea [19]. We have recently adapted the techniques of these authors and developed them to be appropriate for synchrotron research [16,20].

The availability of modern synchrotron radiation brought near-edge absorption of x-rays within the reach of many fields of research. Previously, conventional x-ray diffraction

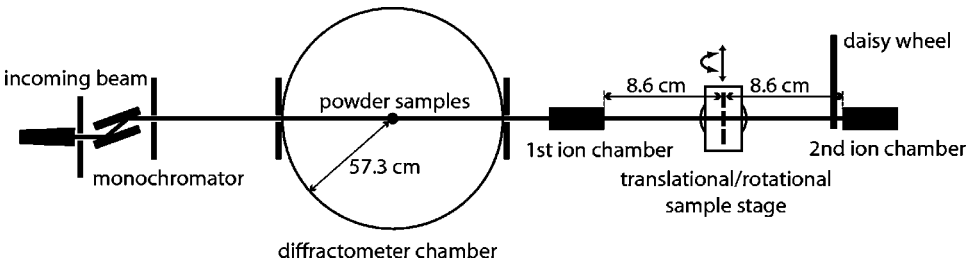

FIG. 1. Experimental setup at beamline 20B, Photon Factory synchrotron, Japan (not to scale).

could not differentiate between metals in different valence states or between consecutive metals in the Periodic Table. However, identification of the absorption edge and near-edge structure allows such distinctions to be observed. The effects of anomalous dispersion find increasing use, and it can be predicted safely that there will soon be a high demand for quantitative data to employ as a major tool in the determination of many properties. For example, multiple-wavelength anomalous dispersion (MAD) [2] now makes it possible to determine the structure of proteins without the need for the heavy metal technique.

These applications invite an accurate set of data on an absolute scale, as presented in this work, which can be used as a reference or calibration for a variety of experiments. In this work we investigate copper, which remains one of the most useful and best tested materials.

II. X-RAY EXTENDED RANGE TECHNIQUE

The x-ray extended range technique uses an extended range of energies, and an extended range of foil thicknesses following an extended range criterion for selection, to address a suite of systematics in x-ray measurements. The technique is directed towards an attenuation measurement, where a sample is interposed between a downstream detector and an upstream monitor in an x-ray beam monochromatized by a double-reflection crystal and collimated by slits. The technique combines normalization, including offsets with the investigation of statistical noise contributions and the optimization of correlation, and accurate and precise attenuation and energy measurement. We give this name to encapsulate the key features of the experimental procedures used in these measurements.

The average thickness of the absorber is determined by weighing a foil whose area has been measured and whose density is known; this corrects for the effects of voids and cracks. The thickness of the thickest absorber is determined in this manner, thus minimizing the relative error in the determination. Other, thinner, foils used at lower x-ray energies are calibrated relative to the thicker foils. The thickness variation of each foil is investigated by scanning it with the x-ray beam used to measure the attenuation.

More than one foil is used to measure the attenuation at each energy. Multiple foils are used to test for the linearity of the counting system and to determine the fraction of harmonics in the x-ray beam. The technique requires measurements over an extended range of energy, and follows a different attenuation criterion for accuracy from that used in the past.

III. EXPERIMENTAL GEOMETRY AND COMPONENTS

Details of our experimental setup are shown in Fig. 1. The incident beam was a bending magnet beam of the Photon Factory synchrotron (beamline 20B) monochromatized by a double reflection from a monolithic silicon 111 monochromator. The monochromator was detuned to minimize higher-order harmonic contributions in the beam [21]. After passing through two apertures which defined the beam size of 1 mm$\times$1 mm with a vertical divergence of 0.12 $\pm$0.03 mrad, the beam passed through a diffractometer (BigDiff) [22] in which powder-diffraction patterns of standard powder specimens Si640b and LaB_6 were used to determine the energy of the x rays. Image plates mounted in the diffractometer covered an angular range from $-80°$ to 120° [22–24]. The angular positions of these image plates were determined precisely from the positions of a set of fiducial marks provided by radioactive sources embedded at calibrated positions in the perimeter of the diffractometer.

The diffractometer was followed by the first of two matched ion chambers (the incident beam monitor); this was followed by a mounting stage holding three foil specimens with a controllable translation for placing the foils in the beam. A separate pair of rotational stages allowed the increase of attenuation with thickness through the sample (on rotation) for aligning the samples exactly perpendicular to the beam. This adjustment is dependent on any sample thickness variation, but we ensured that this latter effect was negligible by taking a range of measurements at large and small angles, rotating around the sample axis, and fitting the result with no observed systematic residual.

The foil mounting stage was followed by a ''daisy wheel'' on whose perimeter were mounted 20 aluminum foils of various thicknesses; these could be inserted into the beam by suitable rotation of the daisy wheel and were used to determine the residual harmonic radiation present in the beam. The daisy wheel was followed by the second ion chamber (the attenuated beam detector). The use of the two matched ion chambers (18 cm effective length, N_2 gas flow) minimized errors arising from source fluctuations and air absorption. Counting statistics were optimized using detailed diagnostics [20].

The copper foils, supplied by Goodfellow, were of thicknesses ranging from 10 μm to 100 μm. The impurity levels of the foils were between 0.01% and 0.03% with typical dominating impurities as follows: lead, $2-100\times10^{-6}$; silver, $4-50\times10^{-6}$; potassium, $1-100\times10^{-6}$; calcium, $1-25\times10^{-6}$. Other contaminants (aluminum, bismuth, bo-

ron, chromium, iron, magnesium, manganese, silicon, sodium, tin) were at a level of less than 10×10^{-6} each.

IV. CALIBRATION FOR THE ATTENUATION COEFFICIENTS IN A SYSTEM USING TWO ION CHAMBERS

The linear absorption coefficient of the sample μ_{sample} can be determined from the Beer-Lambert law. The intensity ratio is corrected for the absorption of the environment $e^{-\mu t_{env}}$ due to air and ion chamber gas and windows by measuring the total attenuation of the environment with the sample (from upstream and downstream ion chamber fluxes I_{up} and I_{down}) and also the attenuation of the environment without the sample in place ($I_{up,0}$ and $I_{down,0}$, where the subscript 0 indicates measurements without a sample attenuating the beam):

$$e^{-(\mu t)_{sample}}=\frac{e^{-[(\mu t)_{env}+(\mu t)_{sample}]}}{e^{-(\mu t)_{env}}} \tag{2}$$

$$=\frac{I_{down}}{I_{up}}\Big/\frac{I_{down,0}}{I_{up,0}}. \tag{3}$$

Detector readings are corrected for the zero offset of the amplifiers. Any reading I with the beam on becomes $I-I_{off}$ after correction for the zero beam offset I_{off}. Hence, the Beer-Lambert formula corrected for normalization and zero offset is

$$(\mu t)_{sample}=\ln\left(\frac{I_{down,0}-I_{down,off}}{I_{up,0}-I_{up,off}}\Big/\frac{I_{down}-I_{down,off}}{I_{up}-I_{up,off}}\right). \tag{4}$$

V. MULTIPLE-FOIL MEASUREMENT

Most experimental work reported previously has been carried out using a single foil chosen to satisfy Nordfors criterion $2<\mu t<4$ [25]. However, these single-foil measurements make it impossible to observe or quantify the harmonic contributions to the x-ray beam, detector linearity, or scattering. Moreover, at low energies and high Z values, for which the appropriate foils are only a few microns thick, use of a single foil results in a large uncertainty in thickness determination.

As shown below, the Nordfors criterion is too constraining and its bounds can be broadened to gain statistical accuracy without requiring unrealistic counting times. We note that the Nordfors criterion is not robust against other systematics arising from harmonic contamination or detector nonlinearity [26].

The incident number of x rays I_{up} required to achieve a given uncertainty of $\%\sigma([\mu/\rho]\rho t)$ is [16]

$$I_{up}=\left(1+\frac{I_{up}}{I_{down}}\right)\left[\left(\frac{1}{\%\sigma_{([\mu/\rho]\rho t)}}\right)\frac{1}{\ln\left(\frac{I_{up}}{I_{down}}\right)}\right]^2, \tag{5}$$

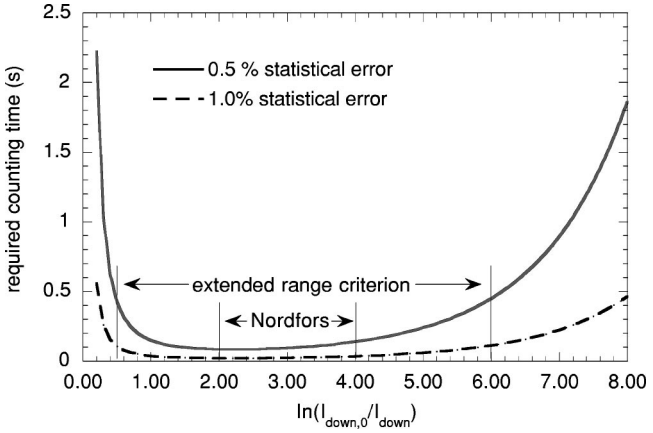

FIG. 2. Optimization of the sample thickness—counting times required to achieve 0.5% and 1% statistical accuracy. The Nordfors criterion was based on the location of the minimum of this curve and not on the effective range for a particular precision. It also does not select optimum ratios in the presence of a wide variety of systematics. The extended range criterion addresses this and allows a range of thicknesses to be used to probe a suite of possible systematic effects.

where $\%\sigma_{([\mu/\rho]\rho t)}$ is the required uncertainty of $([\mu/\rho]\rho t)$, the mass attenuation coefficient is $[\mu/\rho]$, and the density is ρ.

Figure 2 shows the counting time required to achieve 0.5% and 1% statistical precision for a range of attenuation with an incoming flux of 10^6 counts/s, assuming that there is only statistical noise, I_{up} and I_{down} are uncorrelated, and the response of the two ideal ion chamber detectors is perfectly linear. If the foil thickness is chosen such that the logarithm of the intensity ratio $\ln(I_{up}/I_{down})$ is in the range between 0.5 to 6, then, no more than 0.5 second counting time is required to achieve an 0.5% statistical accuracy level. The use of this extended range criterion has made it possible to use multiple foils covering a range of thickness of over an order of magnitude.

In our measurements we used three foils of different thicknesses within the attenuation range $0.5<\mu t<5$ at each energy. The use of samples with μt higher than 5 was limited by the detector linearity range. Ten measurements were carried out for each foil at each energy point (energy steps were 100 to 200 eV away from the absorption edge, and 10 eV near the edge).

VI. INVESTIGATION AND CALIBRATION OF KEY SYSTEMATICS

Although the measurement of the attenuation of x rays by a foil is conceptually simple, in practice considerable care is needed to minimize potential sources of error. This requires the characterization of the thickness and purity of the foils, the monochromaticity and energy of the x-ray beam, the linearity of the detectors and the counting statistics, as well as the determination of contributions due to scattering processes.

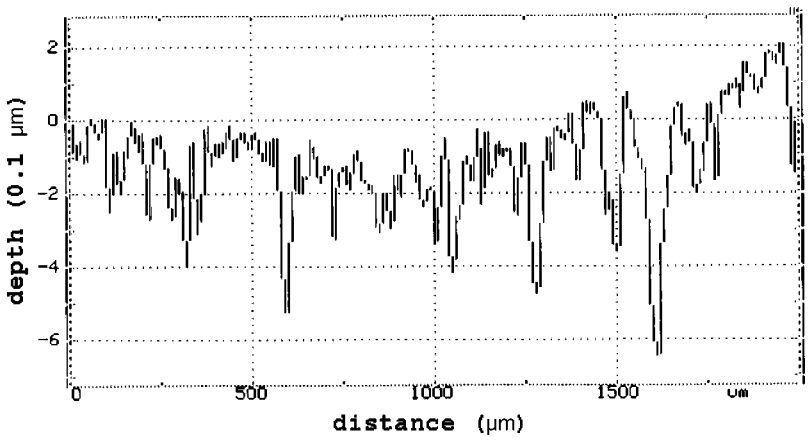

FIG. 3. Profilometer trace showing the microstructure on a surface of the copper foil. The overall curvature is an artifact due to the automatic tilt correction of the profilometer. This microstructure has no effect on the result of the attenuation measurement using our technique, as explained in the text.

A. Foil thickness and uniformity

Uncertainty of the local foil thickness is the most important limitation to the accuracy of the measurement of the attenuation coefficient. In order to satisfy the optimal intensity ratios (the extended range criterion, Fig. 2), the foils used in our experiment ranged in thickness between about 5 and 100 μm.

A combination of methods was employed to determine the foil thickness at the point of incidence of the x-ray beam. The procedure consisted of (1) obtaining the average thickness of the thickest foil by weighing and carefully determining the area of the foil, (2) mapping the thickness of the foil using a micrometer, (3) two-dimensional (2D) mapping of the relative thickness of the central part of the foil using x rays, (4) combining the results of the preceding three measurements, and (5) relating the thicknesses of all other foils to the absolute thickness of the thickest foil by measuring their relative attenuation of x rays.

1. Average thickness of the thickest foil by weighing a known area

The average thickness t_{ave} of the entire foil was determined from $t_{ave}=M/A\rho$, where M is the sample mass, A is the sample surface area, and ρ is the sample density. The mass M ($0.552\,15$ g± 10 μg) was obtained using repeated weighing on a microgram scale (resolution 1 μg), the surface area of the sample $A(657.3\pm 0.25$ mm^2) was measured by using an optical comparator (Mitutogo PJ300 with resolution 5×5 μm^2), and the density ρ used was 8.9331(37) g/cm^3 [27]. The average thickness of the thickest sample obtained was found to be $t_{ave}=94.04\pm 0.05$ μm (0.06% relative accuracy).

The surface of any sample has a significant microstructure, and on the scale of atomic force microscopy and profilometry is quite rough, as seen in Fig. 3 using a Tencor Instruments profilometer along a 2 mm line across the sample in 10 μm steps corresponding to the stylus radius. A determination of the average thickness by mass and area determination automatically corrects for the inevitable microcracks and voids in the copper foil. As seen in the figure, local thickness can vary by 1 μm, and the difference between local thickness and the average thickness can reach 0.5 μm or 0.5%. This makes it crucial to determine the effective local thickness through which the x-ray beam passes rather than an arbitrary or average thickness.

2. Micrometer measurements

The variation in the thickness of the foil was also measured using a micrometer with a 5 mm diameter contact region with 0.5 μm precision at 25 raster points covering the surface. The accuracy and reproducibility of each measurement of thickness was 0.5%, and showed that the variation in local thickness was 1% to 2%. The average thickness of the entire foil obtained by averaging all the micrometer measurements was

$$t_{micro1,ave}=96.2\pm 0.1\ \ \mu\text{m}^2. \tag{6}$$

The micrometer measures the maximum thickness over the area of contact, assuming no deformation of the surface by the measurement. This measurement should be larger than the average thickness obtained from the mass and area, by an amount corresponding to the surface structure variation. This difference is thus consistent with the structure observed in Fig. 3.

3. X-ray two-dimensional mapping

The x-ray 2D measurements are carried out by illuminating an area of 1×1 mm^2—the dimensions of the beam used in the attenuation measurement. To achieve an accuracy that is better than 0.5%, the thickness variation of the thickest foil was also measured by scanning the 20 keV x-ray beam over the central region of the foil in 1 mm steps over an 8×8 mm^2 square area. This provided the most precise relative measure of the local thickness variation,

$$t_{local}=\frac{-\ln\int_0^1\int_0^1 e^{-\mu t(x,y)}dxdy}{\mu}. \tag{7}$$

This measure is directly linked to the attenuation measurements themselves, since it allows for any (negligible) divergence or spatial nonuniformity in the beam and because it covers an area exactly equal to that used in the attenuation measurement itself. This yields a high statistical precision of the relevant local average thickness.

4. Combining the results of the above thickness measurements

We must combine the information from the absolute measurements and the highly precise relative x-ray measurements to yield the absolute thickness over the actual 1×1 mm^2 area through which the beam passed during the attenuation experiment. To achieve this, we carried out the following procedure.

(i) We use an iterative least-squares fitting program to match the xy grids measured with the micrometer and with the X-ray beam in the central 8×8 mm^2 area of the foil, by comparing the thickness variation. After convergence was achieved, the final match was accurate to within an estimated uncertainty of 0.25 mm in each axis for each point which, given the small variation of foil thickness between grid points, was quite adequate.

(ii) Having found the match, we determined the actual thickness of the known 1×1 mm^2 area through which the x-ray beam passed by scaling the relative x-ray measurements to the absolute micrometer measurements.

(iii) It now remained to combine this with the mass average thickness t_{av} which is the most accurate determination of the average thickness of the foil. This was done by comparison of the average thickness of the entire foil from micrometer mapping with t_{av}. The difference of 2.2 μm between these measures was assumed uniform over the foil, and in particular over the central 8×8 mm^2 region probed by the x-ray beam.

The resulting average thickness of the 1×1 mm^2 region through which the x-ray beam passed was 0.09490 ± 0.00026 mm. This 0.27% uncertainty is larger than the 0.06% uncertainty of the average thickness t_{av} and the 0.1% uncertainty of the average micrometer measurement.

5. Determination of the thicknesses of thinner foils

The direct thickness measurements described above were carried out for the thickest foil (100 μm) at the maximum energy of the investigation, where the relative error in the measurement was smallest. The next foil thickness (30 μm) was related to the thickest one by a comparison of their attenuation at the same x-ray energy, where both obeyed our extended range criterion. Thinner foils (20, 15, 10, and 5 μm) were in turn compared using a lower energy x-ray beam. The same size x-ray beam was used in all relative measurements. Hence all thickness measurements were related to the thickest foil whose absolute thickness was determined to high accuracy. This yielded accuracies for thin foils about an order of magnitude higher than previously possible.

Figure 4 shows the consistency of measurements of μ using at least three foils at each energy. The measurements are absolute for the thickest foil. The thicknesses of all other foils were obtained relative to the thickest foil. On each change of foils, at least one foil is retained in the same mounting to facilitate comparison.

B. Effect of impurities and oxidation

Since copper has a relatively low atomic number, the most significant effect of impurity contamination is due to high Z impurities (having higher absorption coefficients). From the impurity levels listed in Sec. III, we assumed the highest-Z elements (Ag, Pb) at the highest possible contaminations (50×10^{-6} and 100×10^{-6}). The systematic shift in the final results due to a contamination by these elements Z_i at corresponding levels C_i% can be calculated from

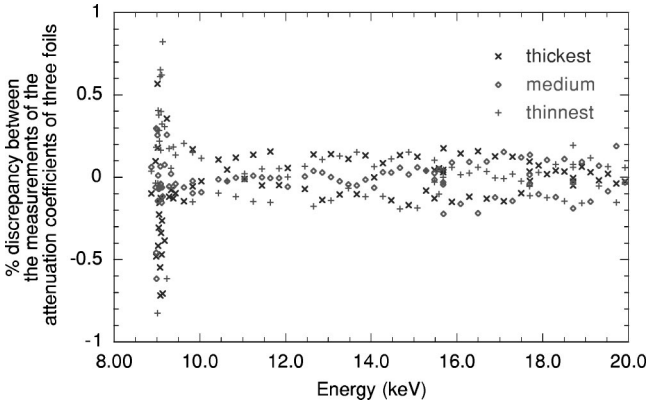

FIG. 4. Percent discrepancy between the attenuation coefficients as measured with three foils of different thickness. The comparatively large error at the absorption edge is due to the high sensitivity of the attenuation coefficients to eV changes in x-ray energy in the region of strong XAFS oscillations. Elsewhere, the discrepancies are 0.2% or less.

$$\%\text{shift}=\frac{\mu_{Cu}\times\text{Cu}\%+\Sigma(\mu_{Z_i}\times C_i\%)}{\mu_{Cu}}. \tag{8}$$

Applying Eq. (8) to the highest Z impurity elements at their maximum possible concentration leads to an insignificant shift of the final results (a maximum shift of 0.013% at 20 keV). In most cases the effect of impurities was much less than this, and more typically it was 0.002%.

The oxide layer on the sample surface was assumed to be about 35 Å thick [28]. Its error contribution is therefore negligible, even for the thinnest 5 μm samples for which it is less than 0.025%. For the thicker foils this contributed less than 0.003%, while for the thickest foil it was approximately 0.001%. The effect of impurities is included in the final columns of Table I, and in the error budget in Table II.

C. X-ray energy calibration

The energy was measured directly at 11 points covering the energy range between 8.85 and 20 keV, and calibrated to the monochromator angle setting over the full range of the experiment. The energy of the x rays was determined from the powder diffraction patterns of the two highest accuracy standard materials: silicon (Si640*b*, $a_0=5.430\,940(11)$ Å [29]) and LaB_6 [$a_0=4.15695(6)$ Å —NIST standard]. Diffraction patterns were recorded using six 20×40 cm^2 image plates with 100 μm (or 0.01° equivalent) resolution. The angular positions of the powder lines on each plate were determined with an accuracy of 0.01° using the precisely known positions of radioactive fiducials located on the inside perimeter of the Australian National Beam-Line Facility diffractometer chamber BL-20B [22–24]. The peak positions

TABLE I. Summary of results for attenuation coefficients $[\mu/\rho]$(cm^2/g) and atomic form factors f_2 versus energy, with errors.

E (keV)	σ_E [a] (eV)	$[\mu/\rho]$ (cm^2/g)	% $\sigma_{\mu,ste}$ [b] (%)	% σ_t [c] (%)	% $\sigma_{\mu,ste}$ + % μ_i [d] (%)	% σ_μ [e] (%)	f_2 [f] (e/atom)	f_2 [g] (e/atom)	σ_{f2} (e/atom)
8.8709	1.02	37.989	0.063	0.332	0.064	0.338	0.4861	0.4866	0.0016
8.9722	0.60	39.368	0.037	0.332	0.037	0.334	0.5089	0.5095	0.0017
8.9824	0.56	174.797	0.585	0.332	0.585	0.673	2.3570	2.3564	0.0159
9.0025	0.49	301.251	0.468	0.332	0.468	0.574	4.0711	4.0699	0.0234
9.0125	0.45	299.160	0.264	0.332	0.264	0.424	4.0473	4.0462	0.0172
9.0225	0.42	280.720	0.072	0.332	0.072	0.340	3.8020	3.8009	0.0129
9.0326	0.38	315.383	0.175	0.332	0.175	0.375	4.2762	4.2750	0.0160
9.0426	0.35	285.828	0.151	0.332	0.151	0.365	3.8797	3.8787	0.0142
9.0526	0.33	289.036	0.132	0.332	0.132	0.357	3.9275	3.9265	0.0140
9.0627	0.30	295.361	0.070	0.332	0.071	0.340	4.0179	4.0169	0.0136
9.0727	0.28	308.366	0.220	0.332	0.220	0.398	4.1994	4.1983	0.0167
9.0827	0.27	311.230	0.312	0.332	0.312	0.456	4.2430	4.2420	0.0193
9.0928	0.26	290.999	0.071	0.332	0.072	0.340	3.9715	3.9706	0.0135
9.1029	0.26	277.705	0.202	0.332	0.202	0.389	3.7943	3.7934	0.0147
9.1129	0.26	285.118	0.265	0.332	0.265	0.425	3.8998	3.8989	0.0166
9.1229	0.28	293.393	0.162	0.332	0.162	0.369	4.0173	4.0164	0.0148
9.1325	0.30	305.582	0.346	0.332	0.346	0.480	4.1886	4.1877	0.0201
9.1828	0.40	290.361	0.127	0.332	0.127	0.355	4.0016	4.0008	0.0142
9.2329	0.30	283.693	0.068	0.332	0.068	0.339	3.9308	3.9301	0.0133
9.2833	0.39	279.171	0.068	0.332	0.068	0.339	3.8890	3.8884	0.0132
9.3334	0.33	270.757	0.030	0.332	0.030	0.333	3.7919	3.7914	0.0126
9.3836	0.33	267.573	0.093	0.332	0.093	0.345	3.7673	3.7668	0.0130
9.4338	0.33	261.422	0.056	0.332	0.056	0.337	3.7001	3.6998	0.0125
9.6343	0.34	245.000	0.083	0.332	0.083	0.342	3.5406	3.5405	0.0121
9.8349	0.31	229.967	0.062	0.332	0.063	0.338	3.3918	3.3918	0.0115
9.8356	0.29	230.996	0.068	0.332	0.068	0.339	3.4072	3.4072	0.0115
10.0362	0.38	217.705	0.059	0.332	0.060	0.337	3.2759	3.2760	0.0111
10.4387	0.30	195.954	0.039	0.332	0.040	0.334	3.0656	3.0658	0.0103
10.6410	0.17	186.096	0.014	0.332	0.015	0.332	2.9671	2.9674	0.0099
10.8417	0.34	176.827	0.043	0.332	0.043	0.335	2.8719	2.8722	0.0096
11.0433	0.34	168.259	0.017	0.332	0.017	0.332	2.7830	2.7832	0.0093
11.2451	0.58	160.321	0.045	0.332	0.045	0.335	2.6996	2.6998	0.0090
11.4464	0.64	152.792	0.030	0.332	0.030	0.333	2.6184	2.6185	0.0087
11.6479	0.73	145.906	0.063	0.332	0.063	0.338	2.5438	2.5439	0.0086
11.8489	0.74	139.292	0.026	0.332	0.027	0.333	2.4699	2.4700	0.0082
12.0510	0.71	133.237	0.020	0.332	0.020	0.333	2.4023	2.4023	0.0080
12.4533	0.72	121.921	0.048	0.332	0.048	0.335	2.2706	2.2705	0.0076
12.6555	0.94	116.835	0.045	0.332	0.046	0.335	2.2107	2.2105	0.0074
12.8570	0.98	111.836	0.075	0.332	0.075	0.340	2.1493	2.1491	0.0073
13.0586	1.17	107.355	0.047	0.332	0.048	0.335	2.0950	2.0947	0.0070
13.2595	0.91	102.906	0.056	0.332	0.056	0.337	2.0387	2.0383	0.0069
13.4607	0.95	98.892	0.045	0.332	0.046	0.335	1.9884	1.9880	0.0067
13.6624	0.91	94.917	0.052	0.332	0.052	0.336	1.9366	1.9362	0.0065
13.8635	1.05	91.348	0.054	0.332	0.054	0.336	1.8908	1.8903	0.0064
14.0651	1.02	87.914	0.024	0.332	0.025	0.333	1.8457	1.8452	0.0061
14.2668	1.13	84.635	0.024	0.332	0.025	0.333	1.8020	1.8013	0.0060
14.4680	1.06	81.430	0.075	0.332	0.075	0.340	1.7577	1.7570	0.0060
14.6698	1.31	78.555	0.036	0.332	0.036	0.334	1.7190	1.7181	0.0057
14.8711	1.47	75.598	0.087	0.332	0.088	0.343	1.6765	1.6756	0.0058
15.0727	1.31	73.016	0.042	0.332	0.042	0.335	1.6407	1.6399	0.0055
15.2741	1.16	70.361	0.053	0.332	0.053	0.336	1.6019	1.6009	0.0054
15.4762	0.62	68.049	0.011	0.332	0.012	0.332	1.5694	1.5683	0.0052

TABLE I. (*Continued*).

E (keV)	σ_E [a] (eV)	$[\mu/\rho]$ (cm^2/g)	$\%\,\sigma_{\mu,ste}$ [b] (%)	$\%\,\sigma_t$ [c] (%)	$\%\sigma_{\mu,ste}+\%\mu_i$ [d] (%)	$\%\,\sigma_\mu$ [e] (%)	f_2 [f] (e/atom)	f_2 [g] (e/atom)	σ_{f2} (e/atom)
15.4764	0.75	67.962	0.070	0.332	0.070	0.339	1.5674	1.5663	0.0053
15.5776	0.91	66.765	0.036	0.332	0.036	0.334	1.5496	1.5486	0.0052
15.6768	0.70	65.683	0.007	0.332	0.009	0.332	1.5340	1.5330	0.0051
15.6768	0.70	65.702	0.012	0.332	0.013	0.332	1.5345	1.5334	0.0051
15.6773	1.46	65.713	0.097	0.299	0.097	0.314	1.5348	1.5337	0.0048
15.8795	1.26	63.409	0.080	0.299	0.081	0.310	1.4997	1.4986	0.0046
16.0817	1.46	61.365	0.072	0.299	0.074	0.308	1.4694	1.4683	0.0045
16.2832	0.87	59.271	0.067	0.299	0.068	0.307	1.4367	1.4355	0.0044
16.4854	1.28	57.361	0.107	0.299	0.108	0.318	1.4073	1.4061	0.0045
16.6875	1.29	55.420	0.058	0.299	0.060	0.305	1.3760	1.3747	0.0042
16.8892	1.10	53.730	0.068	0.299	0.069	0.307	1.3499	1.3485	0.0041
17.0915	1.36	51.960	0.093	0.299	0.094	0.313	1.3207	1.3193	0.0041
17.2929	1.17	50.392	0.072	0.299	0.073	0.308	1.2956	1.2941	0.0040
17.4954	1.45	48.758	0.074	0.299	0.075	0.308	1.2680	1.2664	0.0039
17.6967	0.64	47.393	0.023	0.299	0.026	0.300	1.2464	1.2447	0.0037
17.6967	0.64	47.401	0.048	0.299	0.050	0.303	1.2466	1.2449	0.0038
17.6972	1.26	47.337	0.055	0.271	0.056	0.277	1.2450	1.2432	0.0034
17.8995	1.75	45.875	0.063	0.271	0.064	0.278	1.2200	1.2182	0.0034
18.1004	0.99	44.519	0.042	0.271	0.044	0.275	1.1969	1.1951	0.0033
18.3022	1.03	43.158	0.068	0.271	0.069	0.280	1.1729	1.1711	0.0033
18.5049	1.37	41.913	0.042	0.271	0.044	0.275	1.1514	1.1495	0.0032
18.7054	0.82	40.723	0.031	0.271	0.034	0.273	1.1306	1.1286	0.0031
18.7054	0.82	40.725	0.023	0.271	0.027	0.272	1.1306	1.1286	0.0031
18.7060	1.02	40.682	0.043	0.271	0.045	0.275	1.1295	1.1275	0.0031
18.9061	1.17	39.494	0.050	0.271	0.051	0.276	1.1079	1.1059	0.0031
19.1049	1.53	38.372	0.028	0.271	0.031	0.273	1.0874	1.0853	0.0030
19.3001	1.74	37.318	0.023	0.271	0.027	0.272	1.0681	1.0660	0.0029
19.4919	2.37	36.301	0.018	0.271	0.022	0.272	1.0491	1.0468	0.0029
19.6777	3.14	35.373	0.066	0.271	0.067	0.279	1.0318	1.0295	0.0029
19.8558	4.01	34.525	0.012	0.271	0.017	0.272	1.0159	1.0135	0.0028
20.0286	0.84	33.761	0.034	0.271	0.037	0.274	1.0018	0.9994	0.0027
20.0286	0.84	33.750	0.023	0.271	0.026	0.272	1.0015	0.9991	0.0027

[a]Absolute uncertainty in calibrated energy.

[b]Precision, showing results from repeated measurements at the same energies to illustrate the reproducibility of our measurement.

[c]Percentage accuracy in sample thickness determination.

[d]Percentage precision including uncertainty due to impurity, in quadrature.

[e]Final percentage accuracy.

[f]f_2, after subtraction of the scattering contribution following Chantler [6].

[g]f_2, after subtraction of the scattering contribution following Tran *et al.* [26].

and uncertainties of the lines were determined by a nonlinear least-squares fit of a Lorentzian line and a slowly varying background to the actual data.

A linear least-squares (single-value decomposition) procedure was applied to all the lines of all (six) plates for each of the two powder samples. The fit took into account a constant offset due to the errors in the locations of the plates. The eccentricity of the positions of the powder specimens and the shift in the centroids due to the absorption by the powder specimens were modeled but found to be insignificant. Fitted uncertainties matched the variation observed between fits, arguing that the computation was robust and self-consistent. A separate test was made using fits of individual image plates to assess the self-consistency of local results with the final averages, and to identify any possible outliers.

The resultant energies obtained with the two powder standards were averaged with the weighting derived from the corresponding errors. The energy measurements were carried out at 11 points and the results are summarized in Table III. The energy calibrations using the silicon powder are in good agreement with those using the LaB_6 standard, but we note that the latter results are typically 1.0 ± 0.4 eV higher than the former. Results have investigated absorption corrections to the results of each powder, and these corrections affect the

TABLE II. Summary of the main sources of uncertainties of the mass attenuation coefficient $[\mu/\rho]$, the photoelectric coefficient $[\mu/\rho]_{pe}$, and Im(f) of copper.

Source of uncertainty	% contribution		Notes
	±1 s. d., near edge ~9 keV	above edge 12–20 keV	
Major contributions to precision			
energy drift (on edge)	0.04–0.59		±0.003% to ±0.011% in energy
monochromator hysteresis		<0.06	$\delta E = 1$–4 eV at 19–20 keV
energy calibration elsewhere	0.01–0.03	0.01–0.03	±0.003% to ±0.009% in energy
system statistic	0.02	0.02	reproducibility without sample
Major contributions to accuracy			
experimental precision	0.03–0.59	0.007–0.107	including above contributions
sample thickness	0.33	0.27	with $\delta\rho = 0.04\%$ and thickness transfer
Minor contributions			
impurity contamination	0.002–0.01	0.002–0.01	
oxidation	<0.025	<0.003	35 Å thick layer
detector linearity and harmonic contamination	<0.03	<0.03	
scattering	0.01	0.02	theory and aperture tests
Additional contributions			
For $[\mu/\rho]_{pe}$ and Im(f): Rayleigh scattering	0.075	0.15	variation in theory

derived energies by less than 0.4 eV. This offset between powder results is consistent with the lattice spacing uncertainty for LaB_6 corresponding to (3σ) 0.87 eV at 20 keV and 0.39 eV at 9 keV, compared to 0.12 eV (3σ) uncertainty for the Si standard at 20 keV.

The best fit has an associated uncertainty of 0.14 eV which is remarkably consistent between some 70 peaks on ten independent image plates for two different powder samples. The poorest fit occurs at 14 keV, where the final standard deviation from the mean is 1.0 eV.

To determine energies between these 11 direct measurements, we calibrated the monochromator-controlling encoder using a linear interpolation. The correction to the nominal encoder energy varied between 30 eV at 9 keV and 110 eV at

TABLE III. Energy calibration. Weighted sum and uncertainty of energies measured using Si and LaB_6 powder diffraction samples (with uncertainties given by $\sigma\times\sqrt{\chi^2_{reduced}}$).

Si		LaB_6		Final average	
$E_{w=\sigma\sqrt{\chi^2_r}}$ (keV)	$\sigma\sqrt{\chi^2_r}$ (eV)	$E_{w=\sigma\sqrt{\chi^2_r}}$ (keV)	$\sigma\sqrt{\chi^2_r}$ (eV)	$E_{w=\sigma\sqrt{\chi^2_r}}$ (keV)	$\sigma\sqrt{\chi^2_r}$ (eV)
8.9817	0.38	8.9828	0.35	8.9823	0.56
9.1322	0.40	9.1328	0.35	9.1325	0.29
10.0386	1.23	10.0361	0.19	10.0362	0.37
11.0429	0.39	11.0433	0.16	11.0432	0.14
12.0500	0.37	12.0515	0.26	12.0510	0.70
13.0575	0.45	13.0588	0.26	13.0585	0.56
14.0638	0.40	14.0659	0.30	14.0651	1.01
15.6762	0.36	15.6776	0.39	15.6768	0.70
17.6959	0.59	17.6972	0.51	17.6967	0.64
18.7043	0.61	18.7060	0.47	18.7054	0.82
20.0279	0.55	20.0296	0.62	20.0286	0.84

18.6 keV, fully consistent with the expected encoder performance and clear evidence justifying direct energy calibration in precision experiments. The final energy uncertainty was at most 4.0 eV (0.02%) for the highest energy region (19.4–19.8 keV) over which there was backlash hysteresis due to the change in the direction of rotation of the monochromator. Elsewhere the maximum uncertainty was 1.5 eV.

The vertical divergence of the x-ray beam results in a broadening of the powder diffraction lines, similar to the broadening due to the energy window ΔE. We investigated this, and in all cases the linewidths were consistent with a convolution of widths due to the vertical divergence, the monochromator band pass, the sample width in the beam and the (dominant) image plate reader resolution [30]. This in turn allowed the determination of the energy width or the degree of monochromaticity of the x-ray beam. The energy width was dominated by the 1.5 mm vertical aperture width leading to a significant contribution from divergence. Final estimates from experimental widths varied from 1.6 eV (full width half maximum) to almost 9 eV for the highest 20 keV energies.

D. Linearity of detector response and harmonic contribution to the x-ray beam

Even though the nonlinear behavior of the detector and the contamination of the x-ray beam by harmonics are of different origins, their effect on the final result is similar—a nonlinear relationship between the recorded attenuation $\ln(I_{down}/I_{up})$ and the sample thicknesses. Therefore, testing of the detector linearity and detecting the presence of harmonic contamination in the incident beam must be done for each energy.

In our experiment, the double crystal monochromator was detuned by a solenoid coil pulling on the second face of the channel-cut silicon crystal. A weak link connected these two surfaces, so that the force was sufficient to change the reflection angle of the second monochromator surface with respect to the first, thereby minimizing the higher-order harmonic contamination [26].

The signature of any remaining harmonic contribution and the nonlinear behavior of the detectors were investigated by a series of measurements with 20 thicknesses of aluminum consisting of different numbers of aluminum foils mounted on a daisy wheel. We have shown that harmonic contamination always underestimates the attenuation coefficient, and that a very small percentage contamination with harmonic energies can be detected using this technique [26].

Figure 5 is an example of a combined test of the linearity of detector response and of the absence of harmonic wavelengths in the monochromatized beam. The absence of linearity of this plot of absorption by small numbers of foils would be due to the nonlinear detector response, whereas nonlinearity of the plot for large numbers of foils would indicate the presence of harmonic components in the monochromatized beam [21]. A test such as this was carried out at every energy at which measurements were made. The combined contribution of nonlinearity and harmonic contamination to the measurement error did not exceed 0.02%.

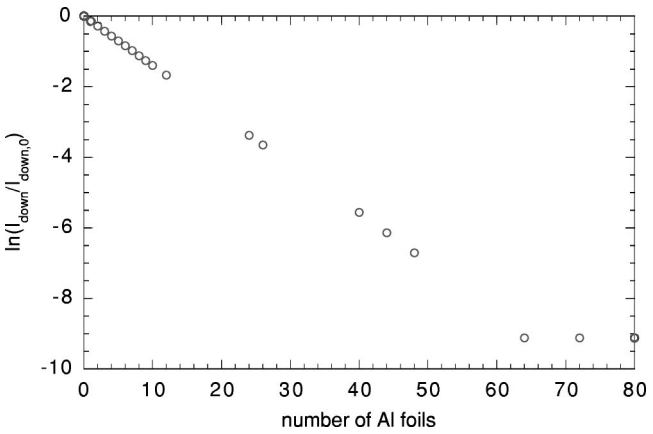

FIG. 5. Measurement of $\ln(I_{down}/I_{down,0}) = -\mu t$ of aluminum as a function of the number of foils in the beam. The linearity of this plot confirms the linearity of the detector response. Linearity for large numbers of foils also confirms the absence of harmonic wavelengths in the monochromatized beam. The slope becomes zero when results are limited by calibration of detector noise and offsets.

E. System statistics

1. Contribution of the system statistics

Counting for longer times at a synchrotron might be expected to solve any problems of counting statistics. However, counting for long times does not necessarily increase statistical precision, due to correlations between counters and any drifts of the beam position with time. Let us define $I_{up,i}$ and $I_{down,i}$ as the two readings of the upstream and downstream ion chambers for measurement i (out of ten measurements at each point) with the beam on and the sample in the beam respectively; $I_{up,i,0}$ and $I_{down,i,0}$ are the two corresponding readings without the sample in the beam; all readings have been corrected for the counting rate observed when the beam was off.

If the fluctuations of the intensity ratios obtained with and without the attenuating samples [Eq. (3)] are uncorrelated, the statistical error of the resultant attenuation coefficient $\sigma_{\mu t}$ is given by

$$\%\sigma_{\mu t}^2 = \%\sigma_{I_{0,down}/I_{0,up}}{}^2 + \%\sigma_{I_{down}/I_{up}}{}^2. \tag{9}$$

However, due to fluctuations in the incident flux, absorption within the ion chambers, etc., the two simultaneous readings from the upstream and downstream ion chambers are correlated. The correlation coefficient contains both positive contributions (e.g., from the fluctuation of the incoming beam) and negative contributions (e.g., from fluctuations of the fractions absorbed in the two ion chambers) and depends strongly on the level of attenuation. This experiment carefully optimized the positive correlation in the signal, which in turn leads to a result of higher precision.

Taking into account the correlation, the statistical uncertainties of the ratios of the upstream and downstream ion chamber readings in Eq. (9) become

$$\%\sigma_{I_{down}/I_{up}}^2 = \%\sigma_{I_{down}}{}^2 + \%\sigma_{I_{up}}{}^2 - 2R\%\sigma_{I_{down}}\%\sigma_{I_{up}}, \tag{10}$$

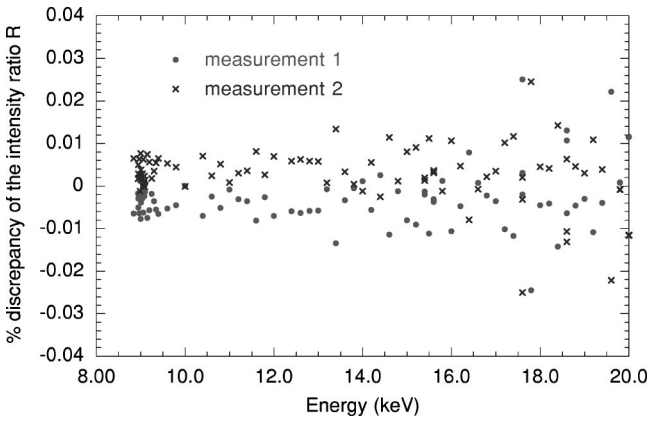

FIG. 6. Reproducibility of direct beam measurements as a function of energy. The discrepancy of the ratio of the detector count divided by the monitor count, compared to the average of the two data sets, is plotted. Note the remarkable consistency at the 0.01% level. This limiting precision may be compared with the consistency of other work, discussed in the text, which typically does not quote a precision better than 1%.

where the correlation coefficient R can be calculated using standard statistical formulas

$$R=\frac{\mathrm{cov}(I_{down},I_{up})}{\sigma_{I_{down}}\sigma_{I_{up}}},$$

$$\mathrm{cov}(I_{down},I_{up})=\frac{1}{n}\sum_{i=1,n}(I_{down,i}-\overline{I}_{down})\times(I_{up,i}-\overline{I}_{up}). \tag{11}$$

$\%\sigma_{I_{up}}$ and $\%\sigma_{I_{down}}$ are the percentage uncertainties of the two incident and attenuated intensities, respectively. More details of the statistics for our experiment are given elsewhere [20].

2. Reproducibility of the measurements

Considerable effort was devoted to exploring causes of discrepancies between the values of $[\mu/\rho]$ obtained with foils of different thickness which appeared to have systematic components. Two sources of error were identified: (i) foils could not be replaced in the holder with complete reproducibility and this resulted in a small variation in the average thickness of the foil exposed to the x-ray beam; (ii) we observed a very slow drift of the monochromator encoder axis after the axis was commanded to stop. This introduced a further uncertainty of about 2 eV to the energy determination. The recognition of these sources of error holds the promise that in future experiments it may be possible to decrease the spread of $[\mu/\rho]$ values in a diagram such as Fig. 4 below the already low present value of about 0.2%.

The reproducibility of the measurements has been tested by comparing the intensity ratios of two series of direct beam measurements of monitor and detector counters over the entire energy range. Fluctuations of $\pm 0.01\%$ have been observed (Fig. 6).

The figure shows the difference between the final intensity ratios after correction for offsets for two independent sets of measurements of the same experimental geometry. Each measurement was composed of 11 consecutive data points which yielded the results for the first and second measurements in remarkable agreement with one another. This result represents a dramatic improvement in precision. The current result is still limited by a systematic contribution, but at a level some two orders of magnitude smaller than in the best results presented in previous literature (for an example of some of the best prior results for precision (1%), but in different systems, see [17–19]; for a review of details of the available literature see [16,31]).

The sample measurements are limited by a similar systematic at a larger level, illustrated by Fig. 4. A systematic is observed due to the energy drift and settling of the monochromator. Except at the absorption edge, the discrepancy is 0.2% or less. The settling behavior, and the corresponding encoder measurements, indicates that the samples measured first are least reliable, but we have included an error estimate based on the full range of deviations. This is the second largest uncertainty in the error budget.

F. Scattering contribution

The Beer-Lambert law relates strictly to photoelectric absorption excluding coherent and incoherent scattering. The introduction of the foil into the x-ray beam typically increased the count rate of the upstream monitor counter by 0.1% due to fluorescence and backscattering from the foil. In order to test the possible effect of this increase of the count rate on the measurement of $[\mu/\rho]$, we compared measurements of $[\mu/\rho]$ obtained when different size apertures were introduced between the sample and both counters. The circular apertures were 3, 6, and 14 mm in diameter and in each measurement identically sized apertures were placed 70 mm on each side of the sample; they were thus about 5 mm from each counter (Fig. 1). The measurements were carried out over the entire energy range of the experiment. The values of $[\mu/\rho]$ obtained with the different apertures differed by no more than 0.08%. This variation was not correlated to the aperture size and there was no effect of aperture size on $[\mu/\rho]$ larger than 0.02%. This result is consistent with modeling based on Rayleigh scattering and fluorescence. Fluorescence and scattering contributions therefore did not affect our results for $[\mu/\rho]$ within our cited error range.

The final accuracy of measured total mass attenuation coefficients is thus 0.3%. Near the K edge the energy uncertainty (and hence the reproducibility of measurements affected by the small energy drift) makes a further contribution.

Extraction of the photoelectric absorption coefficient $[\mu/\rho]_{pe}$ and the imaginary component of the atomic form factor $\mathrm{Im}(f)$ require the subtraction of the contribution from scattering due to the mass scattering coefficient $[\sigma/\rho]$:

$$[\mu/\rho]_{pe}=[\mu/\rho]_{observed,total}-[\sigma/\rho]_{coherent+incoherent}.$$

An experimental upper limit to scattering is given by the backscattering signal, consistent with Rayleigh scattering.

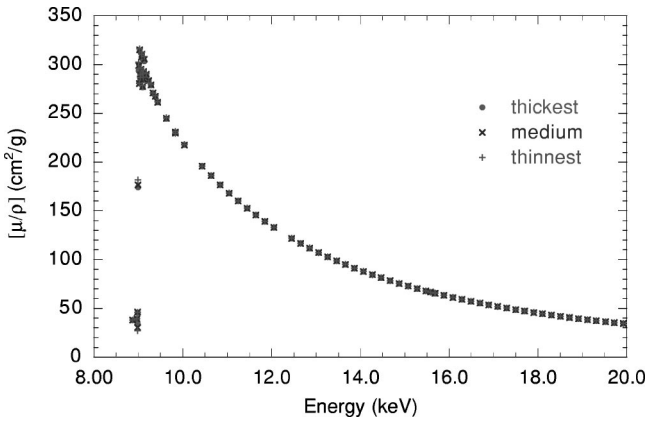

FIG. 7. Results of the measurements of the mass attenuation coefficient of copper. On the scale of this graph the measurements obtained with the three foils thicknesses overlap, showing precision of much better than 1%.

Because scattering contributions for copper are small and primarily due to Rayleigh scattering, theory may be used to subtract off these contributions with an estimated uncertainty equal to half the difference between major tabulations. This then subtracts $0.5\% \pm 0.075\%$ of the total mass attenuation coefficient for energies just above the *K* edge to $2.1\% \pm 0.15\%$ at 20 keV [6,32,7]. The uncertainty in this correction is no more than 0.15%, and makes no significant contribution to measurement uncertainty of $[\mu/\rho]_{total}$ or to the *relative* structure of Im(f) over wide energy ranges.

VII. RESULTS AND DISCUSSION

Figure 7 is a plot of all our measurements as a function of energy. On the scale of this figure, the results obtained with the three foils overlap to well below 1%. The plot is a confirmation of the broad structure expected in this energy range, following the isolated atom approximation or from any of a variety of more detailed theoretical approaches. This type of figure is common in the literature. Such a plot on its own is, however, quite inadequate in illustrating the limitations or strengths of experimental results or their comparison with theory.

Table I is a tabulation of our measurements of the mass absorption coefficient as a function of energy and includes a measure of the precision and accuracy of the experimental determination. It also extracts the corrected value of Im(f) assuming the scattering correction following either Chantler [6], Hubbell and co-workers [32], or Saloman *et al.* [7] as described above. The uncertainty in the last column is a propagation of the error in the previous columns, and does not include an estimate for the uncertainty of the scattering model. Any energy fluctuation or drift, especially near the edge, is listed as an energy uncertainty in Table I, but also adds to the uncertainty in $[\mu/\rho]$ in $\sigma_{\mu,ste}$. Hence our error analysis is conservative.

The experimental edge energy 8.981 keV does not agree with the (simple) theoretical computations and literature value of 8.9789 keV. The discrepancy of 2 eV (corresponding to four standard deviations of the energy determination) is due partly to a definition of the edge energy (is it a turning point, the midpoint of the step, or the onset of the continuum?), partly to theoretical assumptions, and partly to chemical shifts associated with the solid state for copper metal as opposed to the isolated atom prediction.

Table II is a summary of the principal sources of error in the final value of the mass absorption coefficient near the edge and well above the edge, as discussed throughout this paper. While the energy uncertainty is dominant near the edge (column four in Table I), in general the dominant uncertainty is due to the uncertainty in the absolute determination of the thickness of the thickest sample. The thickness transfer method contributes a minor addition to this value (column five of Table I).

The last three columns of Table I give the form factor results after correction for scattering, with the coefficient for Rayleigh and inelastic scattering taken from either [6] or [32,7]. The difference between these two estimates is small compared to the uncertainty in the form factor, and hence this difference makes no significant contribution to the uncertainty.

The form factor is not identical to the atomic form factor, especially near the edge where solid state effects dominate. The form factor reported here is for copper metal, and is not equivalent to that of an isolated atom. We determine Im(f) to be 3.8 ± 0.013 e/atom (electrons/atom) at 9.023 keV and 1 ± 0.003 e/atom at 20 keV, compared to corresponding theoretical values of 3.8 ± 0.38 e/atom and 1.00 ± 0.01 e/atom [6]. This sensitivity in electrons per atom may allow a critical investigation of large contributions to Im(f) from atomic or bound near-edge resonances (XANES), local x-ray absorption fine structure (XAFS), and small relativistic 0.1 e/atom contributions to the real component of the atomic form factor.

Figure 8 shows the discrepancy between various other experimental measurements of the absorption coefficient and the theoretical calculations of Chantler [6]. Our data are in reasonable agreement with Chantler [6], within the 1.0% uncertainty of the theory away from the *K* edge. Theoretical uncertainty increases near the edge. A comparison of our experimental results with theoretical calculations shows discrepancies in the region of the edge, but also in the 16–20 keV range.

The plotted experimental data obtained using laboratory sources [33,34] show significant discrepancies of 4% or 4σ with our results. Reference [34] has an estimated accuracy of 3.7% or some 14 times our estimated accuracy. Reference [33] has an estimated 1% uncertainty but is clearly discrepant, with an estimated accuracy of 5% or 19 times our experimental uncertainty. A further experimental datum [35] lies within 2σ of our results, and has a relatively low quoted error bar of 1% (4 times that of our experimental result). Individual error contributions of this datum have not been reported, and the result has not been discussed in the literature.

Reference [10] is a synchrotron measurement with very high statistical precision, but systematic problems have led to major discrepancies with theory and other experimental work. The authors claim that ''errors in the energy calibra-

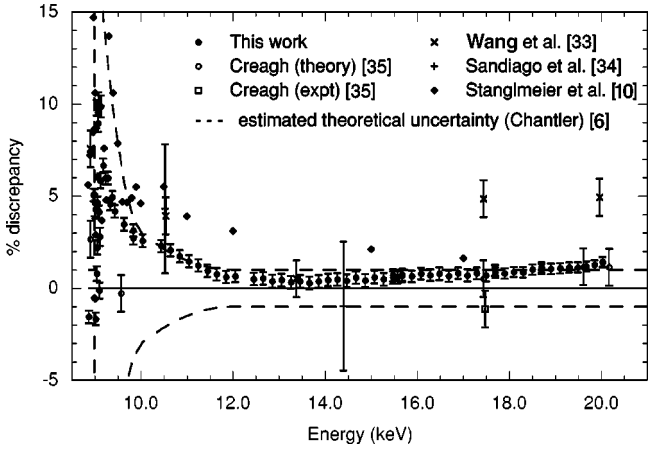

FIG. 8. Comparison between this work and earlier measurements [10,33–35] for copper. Data are compared to theory [6] $\{\% = ([\mu/\rho] - [\mu/\rho]_{theory})/[\mu/\rho]_{theory}\}$, with the theoretical uncertainty given by the region between dashed lines, which increases to 20% near the *K* edge. The comparison of the mass absorption coefficient is identical to that of Im(f) [6]. An alternate theory [35] agrees with the reference theory [6], and agreement of experiment with reference theory is good. The size of diamonds represents the significant figures in [10] (see text).

tion and in the mass absorption coefficient μ/ρ can be neglected'' and quote three significant figures in their results. This may be a statement of statistical precision based on the flux. The experimental data were adjusted to match early theoretical results of Viegele [36] which has an uncertainty exceeding 1%. We note that there remains a discrepancy of 3% between this result and the other experimental measurements and theoretical results in the region. The difference plot (Fig. 8) enables these detailed comparisons to be made.

A more detailed plot in the vicinity of the absorption edge (Fig. 9) shows the expected x-ray absorption fine structure (XAFS). Comparison of our experimental results with the theoretical calculations of Chantler [6] and Scofield [7]

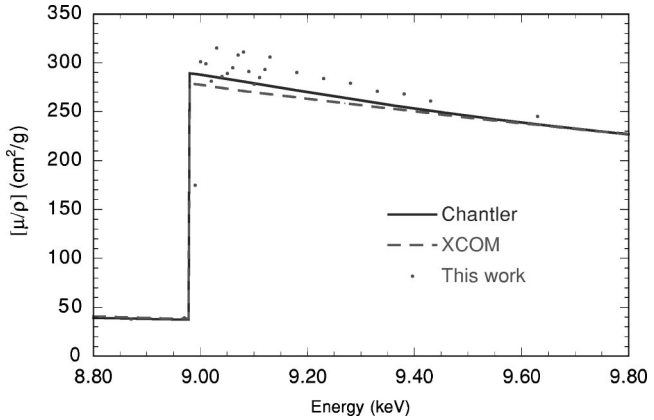

FIG. 9. X-ray anomalous fine structure (XAFS) measurement at the Cu *K* edge on an *absolute* scale, compared to DHF theory (solid line, Chantler [6]) and earlier theory (dashed line, Scofield [7]). The theories do not allow for solid-state effects, but XAFS assumes a baseline underlying the oscillations and [6] provides a more appropriate baseline in this regime.

shows a systematic discrepancy even outside the XAFS region where disagreement is expected because the theories employ the independent particle and isolated atom approximations.

A number of authors have made detailed comparisons of their experimental results with the Scofield theory, which exists in two forms. The first form (unrenormalized) is based on Hartree-Slater orbitals and hence omits certain relativistic corrections. At some level, this limitation would be expected to yield a lower accuracy than, for example, the self-consistent Dirac-Hartree-Fock approach. For $Z=2$ to 54, Scofield provided estimated renormalization factors to convert to values which might be expected from a relativistic Hartree-Fock model. This correction was based primarily on the sum of component orbital electronic amplitudes at the nucleus, and so is not equivalent to a fully relativistic procedure. The differences between renormalized and unrenormalized results vary from 5% to more than 15%.

Scofield's original recommendation was to apply the renormalization correction in all cases. The renormalization correction was not based on a Dirac-Hartree-Fock (DHF) computation but estimated the correction factor for treating the charge density near the nucleus to higher accuracy. Hence this should be a useful correction at high energies for all *Z*. Some reviewers found that this improved agreement with experiment [32]. A decade-long discussion has concerned itself with the relative validity of the renormalized and unrenormalized calculations of a Schrödinger versus Dirac approach. Review authors have concluded that unrenormalized results were superior [7] or that the experimental result lies between the renormalized and unrenormalized calculations [37]. The last statement implies that theoretical error lies in the region of 5–10 %, as opposed to the claimed accuracy of order 0.1–1 % at medium energies. Our experimental results for copper in the 8 to 10 keV region are in much better agreement with DHF theory [6] than with Hartree-Slater theory [7], with or without the renormalization correction. In this work the renormalization correction does not improve agreement with experiment significantly, and a full DHF approach is indicated. However, in the upper energy range, all three of these theoretical results are consistent within their uncertainties.

Figure 10 shows a comparison of our experimental results with the relative measurements of Wong [38]. The fit of these relative measurements to our absolute measurements was carried out by varying three parameters corresponding to Wong's energy scale, relative intensity scale and a parameter which adjusted very slightly the orientation of his plot after it was scanned. The size of the dots representing our measurements is 10σ. The agreement between Wong's curve and our measurements is remarkable.

VIII. SOLID STATE STRUCTURE

EXAFS structure is explained by a combination of accurate relativistic atomic and solid state computations. Modelling of these systems has often used an atomic multiplet approach [39], a local density approximation using infinite crystals (a band structure approach) [40–42], or a cluster

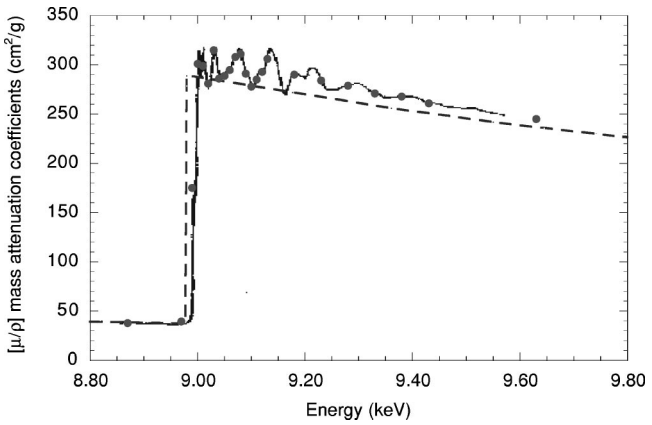

FIG. 10. Detailed XAFS measurement of the Cu *K* edge on an absolute scale, compared to theory (− − −, Chantler [6]). ●, this work (dot size represents 10σ). The relative measurements (—, [38]) are in excellent agreement with our results. Theory based upon the isolated atom approximation serves as a reference profile for XAFS contributions.

approach using multiple scattering theory [3,43]. These codes are contemporaneous with the latest general atomic calculations just discussed, but they are qualitative developments for the interpretation of local structure. Often these solid state computations have been limited to muffin-tin averaging of the potential [44]. The muffin-tin limitations have been lifted in recent years with Koringa-Kohn-Rostoker Green's function methods, various approaches including the full linear augmented plane wave (FLAPW) method, and the finite difference method (FDM) [45,46].

The more generalized potentials are better able to represent local disorder, reflected in the near-edge oscillations. Computations based on a cluster of 13 atoms are quite inadequate and do not represent the local structure. The peaks and structure may be fully converged in such cases, but will often be a poor match even compared to the atomic computation using a fully relativistic code.

A specific direct comparison is provided by the latest result from the FDM formalism [47]. This is plotted against our data in Fig. 11 [48]. The FDM formalism concentrates on the near-edge region from -10 eV to $+60$ eV. The computations have some significant computational cost at energies further away from the edge. Other theoretical predictions (such as the FEFF codes [3]) have greater facility over larger ranges of energy, but there remains significant difficulty in meaningful comparisons outside this range, in part due to the limitations of existing experimental data.

Solid state calculations are extremely relevant and useful in the XAFS region. Many details of the structure are explained by the latest solid state theory. The relative locations of XAFS peaks are well reproduced. It should be remembered that theoretical computations, the relative measurements of Wong, and unpublished, scaled and offset data from ESRF [49] all have a somewhat arbitrary offset in energy, and most have an offset or scaling correction for the edge jump. Core hole widths in this region convolve any sharp structure or sharp edges of theory, which is not uniformly implemented for differing computations. These caveats are continuing areas of serious theoretical research, and so will be strongly motivated by our measurements.

Because of these offsets, we should be comparing relative peak locations of different sources. Only the current work uses an absolute calibration of both energy and attenuation coefficient without offsets or scaling. Other calculations using FLAPW have been reported and also show good agreement with the relative peak locations of the XAFS oscillations [44].

The offsets are much more difficult to compute; far-edge structure and base levels are extremely challenging to estimate using these techniques, and details of the near-edge oscillations await further theoretical developments. An absolute calibration of the local cross section is not a trivial result of current solid state theory, although such theory does a very good job with the edge jump, for example. Compared to the first peak, the second and third experimental peak heights appear to be underestimated by theory, although their locations are fairly well matched.

IX. CONCLUSIONS

The large number and appropriate distribution of our experimental results over the energy range of investigation

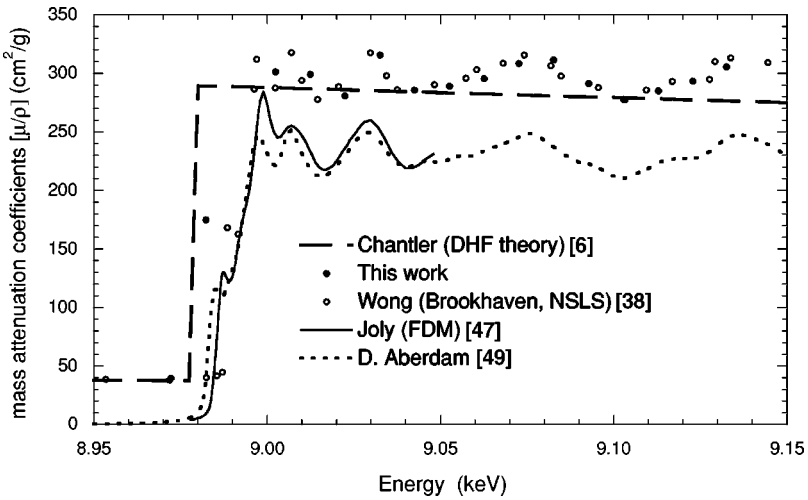

FIG. 11. Detail of the near-edge oscillations at the Cu *K* edge on an *absolute* scale, compared to recent solid state computations using the FDM technique. ●, this work (dot size represents 10σ). This work is in excellent agreement with the relative observations. Locations of peaks are well represented by theory [47], but offsets, background levels, and relative amplitudes of peaks need further theoretical investigation. Relative experimental measurements of Aberdam [49] fail to give accurate edge step heights, edge energies, or scaling, but they give good relative structure for the peak oscillations, which agrees with our absolute results.

(8.84–20 keV) are important features of this work. Our results are among the first of sufficient accuracy to probe and distinguish between alternative theoretical calculations and to quantify solid-state contributions near the Cu $K\alpha$ edge. The data provide high-precision profiles of structure and simultaneously high-accuracy results. This promises to allow observation of small contributions to the near-edge structure (such as purported AXAFS). The data obtained are relevant for MAD, XAFS, and tomographic investigations, in addition to their relevance for the mass attenuation coefficient and atomic form factor in theoretical and experimental investigations.

The x-ray extended range technique is capable of determining the relative structure and absolute values of the photoelectric absorption coefficient and the imaginary component of the atomic form factor with one order of magnitude improvement in accuracy and application over a wider range of energy, and better calibration of all systematics. This provides a direct window into an orbital-by-orbital transform of the electron density. The technique provides an absolute baseline for the quantitative interpretation of XAFS structure, and can compare such a structure with an atomic, isolated atom model to quantitatively investigate atomic resonances and solid state ordering.

In the current experiment, the lower energy results suggest the validity of the DHF approaches to determine wave functions and form factors rather than the Hartree-Slater method. While this may seem obvious, each method involves a range of different assumptions and convergence issues, and previous experimental results have not been of sufficient accuracy to distinguish between these alternatives. The simpler Hartree-Slater method still appears quite reliable in the upper energy range (between 15 keV and 20 keV). The ''renormalization'' procedure is not supported by this experimental data set.

Detailed solid state theory is required to explain details of the structure and oscillations observed in this experiment, although current experimental data appears to challenge even these approaches relating to absolute calibration, background levels and edge steps, and values well away from edges. Further experiments are invited for energies above 20 keV, where deviations between theories again reach several percent. A finer measurement grid near the edge location with the same absolute accuracy as reported would contribute significantly to solid state investigations and to near-edge XAFS studies.

ACKNOWLEDGMENTS

We acknowledge encouragement from D. C. Creagh and R. F. Garrett. The work was performed at the Australian National Beamline Facility with support from the Australian Synchrotron Research Program, funded by the Commonwealth of Australia under the Major National Research Facilities program. We acknowledge the kind assistance of Y. Joly in supplying original theoretical data and the unpublished work of Aberdam *et al.* for reference in this manuscript.

[1] J. M. Bijvoet, Proc. K. Ned. Akad. Wet. **B52**, 313 (1949).
[2] W. A. Hendrikson, Science **254**, 51 (1991); L. K. Templeton and D. H. Templeton, Acta Crystallogr., Sect. A: Found. Crystallogr. **44**, 1045 (1988).
[3] J. J. Rehr, R. C. Albers, and S. I. Zabinsky, Phys. Rev. Lett. **69**, 3397 (1992); D. Sayers, E. Stern, and F. Lytle, *ibid.* **27**, 1204 (1971).
[4] H. Stragier, J. O. Cross, J. J. Rehr, L. B. Sorensen, C. E. Bouldin, and J. C. Woicik, Phys. Rev. Lett. **69**, 3064 (1992).
[5] C. T. Chantler, J. Phys. Chem. Ref. Data **29**, 597 (2000).
[6] C. T. Chantler, J. Phys. Chem. Ref. Data **24**, 71 (1995).
[7] J. H. Scofield, LLNL Report No. UCRI-51326 (1973); E. B. Soloman, J. H. Hubbell, and J. H. Scofield, At. Data Nucl. Data Tables **38**, 1 (1988).
[8] M. Hart and D. P. Siddons, Proc. R. Soc. London, Ser. A **376**, 465 (1981).
[9] D. C. Creagh, Phys. Lett. **103A**, 52 (1984).
[10] F. Stanglmeier, B. Lengeler, W. Weber, H. Göbel, and M. Schuster, Acta Crystallogr., Sect. A: Found. Crystallogr. **48**, 626 (1992).
[11] M. Deutsch and M. Hart, Phys. Rev. B **30**, 640 (1984).
[12] L. K. Templeton and D. H. Templeton, Acta Crystallogr., Sect. A: Found. Crystallogr. **47**, 414 (1991).
[13] Z. Barnea, in *Anomalous Scattering*, edited by S. Ramaseshan and S. C. Abrahams (Munksgaard, Copenhagen, 1975).
[14] P. F. Price, E. N. Maslen, and S. L. Mair, Acta Crystallogr., Sect. A: Found. Crystallogr. **43**, 183 (1987).
[15] P. J. E. Aldred and M. Hart, Proc. R. Soc. London, Ser. A **332**, 223 (1973).
[16] C. T. Chantler, Z. Barnea, C. Q. Tran, J. Tiller, and D. Paterson, Opt. Quantum Electron. **31**, 495 (1999).
[17] D. C. Creagh and J. H. Hubbell, Acta Crystallogr., Sect. A: Found. Crystallogr. **43**, 102 (1987); D. C. Creagh and J. H. Hubbell, *ibid.* **46**, 402 (1990).
[18] L. Gerward, J. Phys. B **22**, 1963 (1989).
[19] J. F. Mika, L. J. Martin, and Z. Barnea, J. Phys. C **18**, 5215 (1985); C. T. Chantler and Z. Barnea, J. Phys.: Condens. Matter **11**, 4087 (1999).
[20] C. T. Chantler, C. Q. Tran, D. Paterson, Z. Barnea, and D. J. Cookson, X-Ray Spectrom. **29**, 449 (2000); **29**, 459 (2000).
[21] G. Materlik and V. O. Kostroun, Rev. Sci. Instrum. **51**, 86 (1980).
[22] Z. Barnea, R. Clapp, D. C. Creagh, T. M. Sabine, A. W. Stevenson, J. W. White, S. W. Wilkins, J. Harada, H. Hashizume, Y. Kashihara, and M. Sakata, K. Ohsumi, and T. Zemb, Rev. Sci. Instrum. **60**, 2537 (1989).
[23] Z. Barnea, D. C. Creagh, T. J. Davis, R. F. Garrett, S. Janky, A. W. Stevenson, and S. W. Wilkins, Rev. Sci. Instrum. **63**, 1069 (1992).
[24] T. M. Sabine, B. J. Kennedy, R. F. Garrett, G. J. Foran, and D. J. Cookson, J. Appl. Crystallogr. **28**, 513 (1995).
[25] B. Nordfors, Ark. Fys. **18**, 37 (1960).

[26] C. Q. Tran, Z. Barnea, M. de Jonge, B. B. Dhal, D. Paterson, D. Cookson, and C. T. Chantler (unpublished).
[27] *Handbook of Chemistry and Physics*, 76th ed., edited by D. R. Lide (CRC Press, London, 1996), pp. 4–139.
[28] F. Stanglemeier, B. Lengeler, and W. Weber, Acta Crystallogr., Sect. A: Found. Crystallogr. **48**, 626 (1992).
[29] *International Tables of Crystallography*, edited by A. J. C. Wilson (Kluwer, Dordrecht, 1995), Vol. 6, p. 429.
[30] D. J. Cookson, J. Synchrotron Radiat. **5**, 1375 (1998).
[31] E. B. Saloman and J. H. Hubbell, Natl. Bur. Stand. (U.S.) Internal Report No. 8 (1986), pp. 86–3431; J. H. Hubbell, Natl. Inst. Stand. Technol. Internal Report No. 5437 (1994).
[32] J. H. Hubbell and I. Överbö, J. Phys. Chem. Ref. Data **8**, 69 (1979); D. Schaupp, M. Schumacher, F. Smend, P. Rulhusen, and J. H. Hubbell, *ibid.* **12**, 467 (1983).
[33] D. Wang, X. Ding, X. Wang, H. Yang, H. Zhou, X. Shen, and G. Zhu, Nucl. Instrum. Methods Phys. Res. B **71**, 241 (1992).
[34] T. K. U. Sandiago and R. Gowda, Pramana, J. Phys. **48**, 1077 (1997).
[35] D. C. Creagh and W. McAuley, *International Table for X-ray Crystallography*, edited by A. J. C. Wilsons (Kluwer Academic, Doredrecht, 1995), Vol. C, Sec. 4.2.6, p. 206; D. C. Creagh and J. H. Hubbell, *ibid.* Sec. 4.2.4, pp. 189–206.
[36] Wm. J.Viegele;, At. Data **5**, 51 (1973).
[37] L. Gerward, J. Phys. B **22**, 1963 (1989); Nucl. Instrum. Methods Phys. Res. B **69**, 407 (1992).
[38] J. Wong, *Reference X-ray Spectra of Metal Foils*, EXAFS Materials, Inc., 871 El Cerro Blvd, Danville CA (1999). These results have a very fine grid giving the local structure with greater detail than most published results. These data, after scaling to give absolute results, are excellent for testing reproducibility of structure in XAFS.
[39] F. M. F. de Groot, J. Electron Spectrosc. Relat. Phenom. **62**, 111 (1993); C. De Nadai, A. Demourgues, J. Grannec, and F. M. F. de Groot, Phys. Rev. B **63**, 125123 (2001).
[40] G. Doolen and D. A. Liberman, Phys. Scr. **36**, 77 (1987).
[41] L. F. Mattheiss and R. E. Dietz, Phys. Rev. B **22**, 1663 (1980).
[42] D. A. Muller, Ultramicroscopy **78**, 163 (1999).
[43] T. A. Tyson, K. O. Hodgson, C. R. Natoli, and M. Benfatto, Phys. Rev. B **46**, 5997 (1992); A. Gonis, X.-G. Zhang, and D. M. Nicholson, Phys. Rev. B **40**, 947 (1989).
[44] J. E. Muller, O. Jepsen, and J. W. Wilkins, Solid State Commun. **42**, 365 (1982).
[45] P. Rez, J. R. Alvarez, and C. Pickard, Ultramicroscopy **78**, 175 (1999).
[46] Y. Joly, Phys. Rev. B **53**, 13 029 (1996).
[47] Y. Joly, Phys. Rev. B **63**, 125120 (2001).
[48] Y. Joly (private communication).
[49] D. Aberdam *et al.*, European Synchrotron Research Facility (unpublished).